# A Rydberg quantum simulator

Hendrik Weimer[1]*, Markus Müller[2], Igor Lesanovsky[2,3], Peter Zoller[2] and Hans Peter Büchler[1]

A universal quantum simulator is a controlled quantum device that reproduces the dynamics of any other many-particle quantum system with short-range interactions. This dynamics can refer to both coherent Hamiltonian and dissipative open-system evolution. Here we propose that laser-excited Rydberg atoms in large-spacing optical or magnetic lattices provide an efficient implementation of a universal quantum simulator for spin models involving $n$-body interactions, including such of higher order. This would allow the simulation of Hamiltonians of exotic spin models involving $n$-particle constraints, such as the Kitaev toric code, colour code and lattice gauge theories with spin-liquid phases. In addition, our approach provides the ingredients for dissipative preparation of entangled states based on engineering $n$-particle reservoir couplings. The basic building blocks of our architecture are efficient and high-fidelity $n$-qubit entangling gates using auxiliary Rydberg atoms, including a possible dissipative time step through optical pumping. This enables mimicking the time evolution of the system by a sequence of fast, parallel and high-fidelity $n$-particle coherent and dissipative Rydberg gates.

Laser-excited Rydberg atoms[1–7] stored in large-spacing optical lattices[8] or magnetic trap arrays[9] offer unique possibilities for implementing scalable quantum information processors. In such a set-up single atoms can be loaded and kept effectively frozen at each lattice site, with long-lived atomic ground states representing qubits or effective spin degrees of freedom. Lattice spacings of the order of a few micrometres allow single-site addressing with laser light, and thus individual manipulation and readout of atomic spins. Exciting atoms with lasers to high-lying Rydberg states and exploiting the strong and long-range dipole–dipole or van der Waals interactions between Rydberg states provides fast and addressable two-qubit entangling operations or effective spin–spin interactions; recent theoretical proposals have extended Rydberg-based protocols towards a single step, high-fidelity entanglement of a mesoscopic number of atoms[10,11]. Remarkably, the basic building blocks behind such a set-up have been demonstrated recently in the laboratory by several groups[12,13].

Motivated by and building on these new experimental possibilities, we discuss below a Rydberg quantum simulator for many-body spin models. As a key ingredient of our set-up (see Fig. 1) we introduce extra auxiliary qubit atoms in the lattice, which have a twofold role. First, they control and mediate effective $n$-body spin interactions among a subset of $n$ system spins residing in their neighbourhood of the lattice. In our scheme this is achieved efficiently, making use of single-site addressability and a parallelized multi-qubit gate, which is based on a combination of strong and long-range Rydberg interactions and electromagnetically induced transparency, as suggested recently in ref. 11. Second, the auxiliary atoms can be optically pumped, thereby providing a dissipative element, which in combination with Rydberg interactions results in effective collective dissipative dynamics of a set of spins located in the vicinity of the auxiliary particle, which itself eventually factors out from the system spin dynamics. The resulting coherent and dissipative dynamics on the lattice can be represented by, and thus simulates a master equation $\dot{\rho} = -(i/\hbar)[H, \rho] + \mathcal{L}\rho$ (ref. 14), where the Hamiltonian $H = \sum_\alpha H_\alpha$ is the sum of $n$-body interaction terms, involving a quasi-local collection of spins in the lattice. The Liouvillian

term $\mathcal{L} = \sum_\beta \mathcal{D}(c_\beta)$ with $\mathcal{D}(c)\rho = c\rho c^\dagger - (1/2)c^\dagger c \rho - \rho(1/2)c^\dagger c$ in the Lindblad form governs the dissipative time evolution, where the many-particle quantum jump operators $c_\beta$ involve products of spin operators in a given neighbourhood.

The actual dynamics of our system is carried out as a stroboscopic sequence of coherent and dissipative operations involving the auxiliary Rydberg atoms over time steps $\tau$, with the master equation emerging as a coarse-grained description of the time evolution. For purely coherent dynamics governed by the Hamiltonian, this is the familiar 'digital quantum simulator[15,16]', where for each time step the evolution operator is implemented through a Trotter expansion $e^{-iH\tau/\hbar} \approx \prod_\alpha e^{-iH_\alpha\tau/\hbar}$ and a certain error associated with the non-commutativity of the quasi-local interactions $H_\alpha$. The concept of stroboscopic time evolution is readily adapted to the dissipative case by interspersing coherent propagation and dissipative time steps $e^{\mathcal{L}\tau} \approx \prod_\beta e^{\mathcal{D}(c_\beta)\tau}$, providing an overall simulation of the master equation by sweeping over the whole lattice with our coherent and dissipative operations. Many of these steps can in principle be done in a highly parallel way, rendering the time for a simulation step independent of the system size. In our scheme, the characteristic energy scale of the many-body interaction terms is essentially the same for two-body, four- or higher-order interaction terms, and mainly limited by the fast timescale to carry out the parallel mesoscopic Rydberg gate operations.

## Coherent and dissipative many-body spin dynamics

Before proceeding with the concrete physical implementation of our Rydberg quantum simulator, we find it convenient to discuss special spin models and master equations of interest, starting with an explicit example: Kitaev's toric code. We will discuss the realization of a more complex set-up of a three-dimensional $U(1)$ lattice gauge theory, giving rise to a spin-liquid phase, in the last section.

Kitaev's toric code is a paradigmatic, exactly solvable model, out of a large class of spin models, which have recently attracted a lot of interest in the context of studies on topological order and quantum
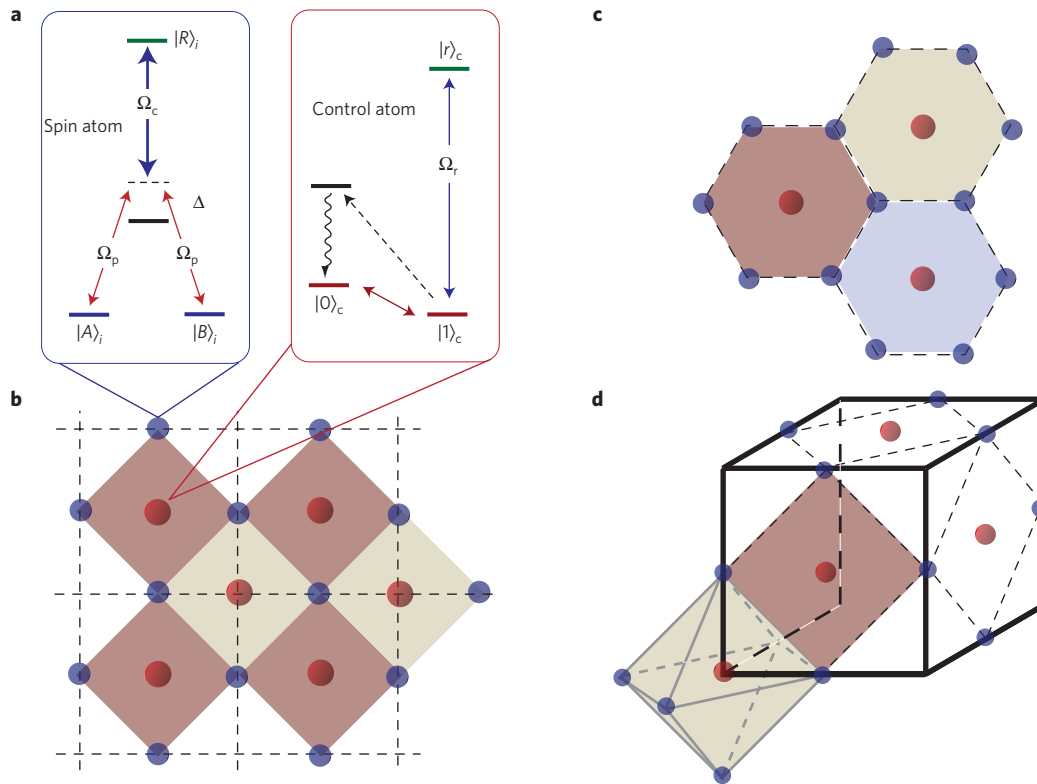
**Figure 1 | Set-up of the system. a**, Two internal states $|A\rangle_i$ and $|B\rangle_i$ give rise to an effective spin degree of freedom. These states are coupled to a Rydberg state $|R\rangle_i$ in two-photon resonance, establishing an electromagnetically induced transparency condition. On the other hand, the control atom has two internal states $|0\rangle_c$ and $|1\rangle_c$. The state $|1\rangle_c$ can be coherently excited to a Rydberg state $|r\rangle_c$ with Rabi frequency $\Omega_r$, and can be optically pumped into the state $|0\rangle_c$ for initializing the control qubit. **b**, For the toric code, the system atoms are located on the links of a two-dimensional square lattice, with the control qubits in the centre of each plaquette for the interaction $A_p$ and on the sites of the lattice for the interaction $B_s$. **c,d**, Set-up required for the implementation of the colour code (**c**) and the $U(1)$ lattice gauge theory (**d**).

computation. It considers a two-dimensional set-up, where the spins are located on the edges of a square lattice[17]. The Hamiltonian $H = -E_0(\sum_p A_p + \sum_s B_s)$ is a sum of mutually commuting stabilizer operators $A_p = \prod_{i \in p} \sigma_i^x$ and $B_s = \prod_{i \in s} \sigma_i^z$, which describe four-body interactions between spins located around plaquettes ($A_p$) and vertices ($B_s$) of the square lattice (see Fig. 1b). The ground state of the Hamiltonian is the simultaneous eigenstate of all stabilizer operators $A_p$ and $B_s$ with eigenvalues $+1$, and gives rise to a topological phase: the ground-state degeneracy depends on the boundary conditions and topology of the set-up, and the elementary excitations obey anyonic statistics under braiding. The toric code shows two types of excitation corresponding to $-1$ eigenstates of each stabilizer $A_p$ ('magnetic charge') and $B_p$ ('electric charge').

A dissipative dynamics that 'cools' into the ground-state manifold is provided by a Liouvillian with quantum jump operators,

$$c_p = \frac{1}{2}\sigma_i^z[1 - A_p], \quad c_s = \frac{1}{2}\sigma_j^x[1 - B_s] \quad (1)$$

with $i \in p$ and $j \in s$, which act on four spins located around plaquettes p and vertices s, respectively. The jump operators are readily understood as operators that 'pump' from $-1$ into $+1$ eigenstates of the stabilizer operators: the part $(1 - A_p)/2$ is a projector onto the eigenspace of $A_p$ with $-1$ eigenvalue, whereas all states in the $+1$ eigenspace are dark states. The subsequent spin flip $\sigma_j^x$ transfers the excitation to the neighbouring plaquette. The jump operators then give rise to a random walk of anyonic excitations on the lattice, and whenever two excitations of the same type meet they are annihilated, resulting in a cooling process, see Fig. 2. Similar arguments apply to $c_s$. Efficient cooling is achieved by alternating the index $i$ of the spin that is flipped.

Our choice of the jump operator follows the idea of reservoir engineering of interacting many-body systems, as discussed in refs 18,19. In contrast to alternative schemes for measurement-based state preparation[20], here, the cooling is part of the time evolution of the system. These ideas can be readily generalized to more complex stabilizer states and to set-ups in higher dimensions, as in, for example, the colour code[21] (see Fig. 1c). As a final remark, we would like to mention that the toric code can also be derived as a perturbative limit of a Hamiltonian with two-body interactions on a honeycomb lattice[22], of which implementations have been suggested both for cold atoms[23] and condensed-matter systems[24]. In our approach, the higher-order interactions arise in a non-perturbative way and the scheme also allows for dissipative state preparation.

## Implementation of a single time step

We now turn to the physical implementation of the digital quantum simulation. The system and auxiliary atoms are stored in a deep optical lattice or magnetic trap arrays with one atom per lattice site, where the motion of the atoms is frozen and the remaining degree of freedom of the system and auxiliary atoms are effective spin-1/2 systems described by the two long-lived ground states $|A\rangle_i$ and $|B\rangle_i$ and $|0\rangle_c$ and $|1\rangle_c$, respectively (see Fig. 1a). We first discuss the elements of the digital quantum simulator for a small local set-up, and present the extension to the macroscopic lattice system below. To be specific, we will focus on a single plaquette in the example of Kitaev's toric code outlined above.

The implementation of the four-body spin interaction $A_p = \prod_i \sigma_i^x$ and the jump operator $c_p$ uses an auxiliary qubit located at the centre of the plaquette (see Fig. 1b). The general
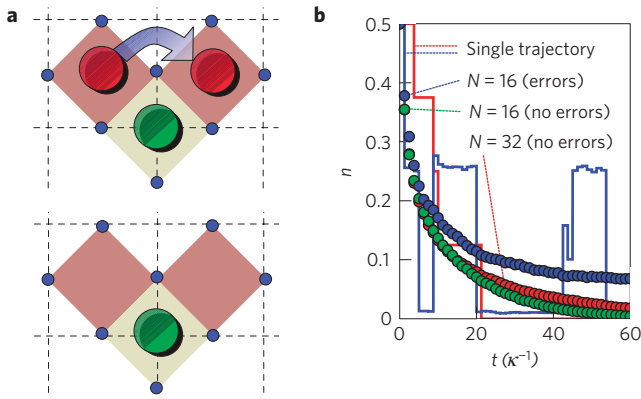
**Figure 2 | Cooling of the toric code. a**, A dissipative time step moves one anyonic excitation (red dot) on top of a second anyon sitting on a neighbouring plaquette, annihilating each other and thus lowering the internal energy of the system. The anyon of different type (green dot) is unaffected as moves of anyons occur only with a small probability. **b**, Numerical simulation of the cooling for $N$ lattice sites (periodic boundary conditions). Single trajectories for the anyon density $n$ over time are shown as solid lines. Filled circles represent averages over 1,000 trajectories. The initial state for the simulations is the fully polarized, experimentally easily accessible state of all spins down. For perfect gates the energy of the system reaches the ground-state energy in the long time limit, whereas for imperfect gates heating events can occur (blue solid line) and a finite density of anyons $n$ remains present (blue circles). In this example the phase shift determining the cooling rate was set to $\theta = 1.25$, providing a characteristic timescale $\kappa^{-1} \sim 8\,\mu s$, and the parameter quantifying the gate error was $|Q| = 0.1$ (see the Methods section for details).

approach then consists of three steps (see Fig. 3b). We first carry out a gate sequence $G$, which encodes the information whether the four spins are in a $+1$ or $-1$ eigenstate of $A_p$ in the two internal states of the auxiliary atom. As a second step, we apply gate operations that depend on the internal state of the control qubit. As a result of the previous mapping, these manipulations of the control qubit are equivalent to manipulations on the subspaces with fixed eigenvalues of $A_p$. Finally, the mapping $G$ is reversed, and the control qubit is reinitialized incoherently in its internal state $|0\rangle$ by optical pumping.

The mapping $G$ is a sequence of three gate operations

$$G = U_c(\pi/2)^{-1} U_g U_c(\pi/2)$$

where $U_c(\pi/2) = \exp(-i\pi\sigma_y/4)$ is a standard $\pi/2$ single-qubit rotation of the control qubit and the parallelized many-body Rydberg gate[11] takes the form (see Fig. 1a for the required electronic level scheme and the Methods section for a brief summary)

$$U_g = |0\rangle\langle0|_c \otimes \mathbf{1} + |1\rangle\langle1|_c \otimes \prod_{i\in p} \sigma_i^x \qquad (2)$$

For the control qubit initially prepared in $|0\rangle_c$, the gate $G$ coherently transfers the control qubit into the state $|1\rangle_c$ ($|0\rangle_c$) for any system state $|\lambda, -\rangle$ ($|\lambda, +\rangle$), with $|\lambda, \pm\rangle$ denoting the eigenstates of $A_p$, that is, $A_p|\lambda, \pm\rangle = \pm|\lambda, \pm\rangle$, see Fig. 3.

For the coherent time evolution, the application of a phase shift $\exp(i\phi\sigma_c^z)$ on the control qubit and the subsequent reversion of the gate, $G^{-1}$, implements the time evolution according to the many-body interaction $A_p$, that is,

$$U_{\rm int} = \exp\left(i\phi A_p\right) = G^{-1} \exp\left(i\phi\sigma_c^z\right) G$$

The control qubit returns to its initial state $|0\rangle_c$ after the complete sequence and, therefore, effectively factors out from the dynamics of the system spins. For small phase imprints, $\phi \ll 1$, the mapping reduces to the standard equation for coherent time evolution

$$\partial_t \rho = -\frac{i}{\hbar} E_0 \left[-A_p, \rho\right] + o(\phi^2)$$

The energy scale for the four-body interaction $A_p$ becomes $E_0 = \hbar\phi/\tau$, with $\tau$ being the time required for the implementation of a single time step.

On the other hand, for the dissipative dynamics, we are interested in implementing the jump operator $c_p$ (see equation (1)). For this purpose, after the mapping $G$, we apply a controlled spin flip onto one of the four system spins,

$$U_{Z,i}(\theta) = |0\rangle\langle0|_c \otimes \mathbf{1} + |1\rangle\langle1|_c \otimes \Sigma$$

with $\Sigma = \exp(i\theta\sigma_i^z)$. As desired, the sequence $G^{-1} U_{Z,i}(\theta) G$ leaves the low-energy sector $|\lambda, +\rangle$ invariant, as these states are mapped onto $|0\rangle_c$ and are therefore unaffected by $U_{Z,i}(\theta)$. In contrast—with a certain probability—the sequence carries out a controlled spin flip on the states $|\lambda, -\rangle$. Once a spin is flipped, the auxiliary qubit remains in the state $|1\rangle_c$, and optical pumping from $|1\rangle_c$ to $|0\rangle_c$ is required to reinitialize the system, guaranteeing that the control qubit again factors out from the system dynamics. The optical pumping constitutes the dissipative element in the system and enables one to remove entropy to cool the system. Note that although optical pumping may lead to heating of the motional degrees of freedom, it is possible to recool the control atom afterwards, for example, by sideband cooling. The two-qubit gate $U_{Z,i}(\theta)$ is implemented in close analogy to the many-body Rydberg gate $U_g$ previously discussed. For small phases $\theta$ the operator $\Sigma$ can be expanded, and the density matrix $\rho$ of the spin system evolves in one dissipative time step according to the Lindblad form

$$\partial_t \rho = \kappa \left[ c_p \rho c_p^\dagger - \frac{1}{2}\left\{c_p^\dagger c_p \rho + \rho c_p^\dagger c_p\right\} \right] + o(\theta^3)$$

with the jump operators $c_p$ given in equation (1) and the cooling rate $\kappa = \theta^2/\tau$. Note, that the cooling also works for large phases $\theta$, and therefore the most efficient dissipative state preparation is achieved with $\theta = \pi$.

The above scheme for the implementation of the many-body interaction $A_p$ and the dissipative cooling with $c_p$ can be naturally extended to arbitrary many-body interactions between the system spins surrounding the control atom, as for example, the $B_p$ interaction terms in the above toric code. Gate operations on single system spins enable us to transform $\sigma_i^x$ into $\sigma_i^y$ and $\sigma_i^z$, in accordance with previous proposals for digital simulation of spin Hamiltonians[25], and selecting only certain spins to participate in the many-body gate, through local addressability, gives rise to the identity operator for the non-participating spins. Consequently, we immediately obtain the implementation of the general many-body interaction and jump operators

$$A_\alpha = \prod_i W_i, \quad c_\beta = \frac{1}{2}Q_i\left[1 - \prod_j W_j\right] \qquad (3)$$

with $W_i, Q_i \in \{1, \sigma_i^x, \sigma_i^y, \sigma_i^z\}$. Here, $\alpha$ and $\beta$ stand for a collection of indices characterizing the position of the local interaction and the interaction type. Note that $A_\alpha$ also includes single-particle terms, as well as two-body interactions.

## Toolbox for digital quantum simulation

Extending the analysis to a large lattice system with different, possibly non-commuting interaction terms in the Hamiltonian, that is, $H = \sum_{\alpha} E_{\alpha} A_{\alpha}$ and dissipative dynamics described by a set of jump operators $c_{\beta}$ with damping rates $\kappa_{\beta}$, provides a complete toolbox for the quantum simulation of many-body systems. Each term is characterized by a phase $\phi_{\alpha}$ ($\theta_{\beta}$) written during a single time step determining its coupling energy $E_{\alpha} = \hbar \phi_{\alpha}/\tau$ and damping rate $\kappa_{\beta} = \theta_{\beta}^2/\tau$. For small phases $\phi_{\alpha} \ll 1$ and $\theta_{\beta} \ll 1$, the sequential application of the gate operations for all interaction and damping terms reduces to a master equation of the Lindblad form,

$$\partial_t \rho = -\frac{i}{\hbar}[H, \rho] + \sum_{\beta} \kappa_{\beta} \left[ c_{\beta} \rho c_{\beta}^{\dagger} - \frac{1}{2}\left(c_{\beta}^{\dagger} c_{\beta} \rho + \rho c_{\beta}^{\dagger} c_{\beta}\right) \right]$$

The choice of the different phases during each time step allows for the control of the relative interaction strength of the different terms, as well as the simulation of inhomogeneous and time-dependent systems.

The characteristic energy scale for the interactions $E_{\alpha}$ and damping rates $\kappa_{\beta}$ are determined by the ratio between the timescale $\tau$ required to carry out a single time step, and the phase difference $\phi_{\alpha}$ and $\theta_{\beta}$ written during these time steps. It is important to stress that in our set-up, the interactions are quasi-local and influence only the spins surrounding the control qubit. Consequently, the lattice system can be divided into a set of sublattices on which all gate operations that are needed for a single time step $\tau$ can be carried out in parallel. Then, the timescale for a single step $\tau$ becomes independent of the system size and is determined by the product of the number $z$ of such sublattices and the duration $\tau_s$ of all gate operations on one sublattice. In our set-up, $\tau_s$ is mainly limited by the duration of the many-body Rydberg gate $U_g$, which is on the order of $\sim 1\,\mu s$ (see the Methods section for details). For the toric code discussed above, we have to apply the many-body gate twice for every interaction term (see Fig. 3), and with $z = 4$, we obtain $\tau$ of a few microseconds, resulting in characteristic energy scales and cooling rates of the order of hundreds of kilohertz. For the simulation of Hamiltonian dynamics this energy scale may be lower if Trotterization errors have to be taken care of. It is a crucial aspect of this quantum simulation with Rydberg atoms that it can be carried out quickly and is compatible with current experimental timescales of cold atomic gases[26].

Finally, we would like to point out that imperfect gate operations provide, in leading order, small perturbations for the Hamiltonian dynamics and weak dissipative terms; see the Methods section and Fig. 2 for a numerical analysis of the induced errors. However, the thermodynamic properties and dynamical behaviour of a strongly interacting many-body system are in general robust to small perturbations in the Hamiltonian; for example, the stability of the toric code for small magnetic fields has recently been demonstrated[27]. Consequently, small imperfections in the implementation of the gate operations are tolerable.

An important aspect for the characterization of the final state is the measurement of the correlation functions $\chi = \langle A_{\alpha_1} \cdots A_{\alpha_n} \rangle$, where $A_{\alpha_j}$ denote local, mutually commuting many-body observables. In our scheme, the observables $A_{\alpha_j}$ can be measured through the mapping $G$ of the system information onto auxiliary qubits and their subsequent state-selective detection. In analogy to noise correlation measurements in cold atomic gases[28,29], the repeated measurement with such a detection scheme provides the full distribution function for the observables, and therefore enables one to determine the correlation function $\chi$ in the system. Consequently, in the above discussion of Kitaev's toric code, the necessary string operators characterizing topological order can be detected.
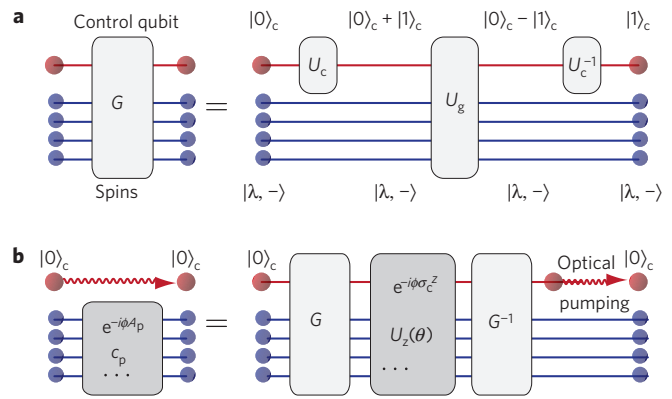


**Figure 3 | Single time step. a**, The gate sequence $G$ coherently maps the information whether the system spins reside in any eigenstate $|\lambda, -\rangle$ ($|\lambda, +\rangle$) corresponding to the eigenvalue $-1$ ($+1$) of the many-body interaction $A_p$ onto the internal state $|1\rangle_c$ ($|0\rangle_c$) of the control qubit. **b**, After the mapping $G$, we apply gate operations, which depend on the internal state of the control qubit. Finally, the mapping $G$ is reversed and the control qubit is incoherently reinitialized in state $|0\rangle_c$ by optical pumping. At the end of the complete sequence the dynamics of the control qubit factors out.
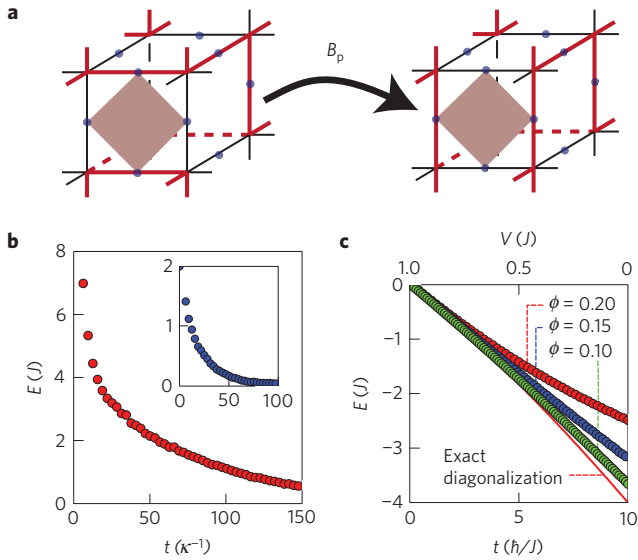
## Lattice gauge theory

In the first example, we discussed the implementation of the quantum simulator for the toric code, and the extension to more complex stabilizer states is straightforward. In the following, we will show that our approach can also be extended to systems with non-commuting terms in the Hamiltonian. As an example, we focus on a three-dimensional $U(1)$ lattice gauge theory[30], and show that dissipative ground-state cooling can also be achieved in such complex models. Such models have attracted a lot of recent interest in the search for 'exotic' phases and spin liquids[31–34]. The three-dimensional set-up consists of spins located on the links of a cubic lattice (see Fig. 1d). The lattice structure for the spins can be viewed as a corner-sharing lattice of octahedra with one site of the cubic lattice in the centre of each octahedron. The Hamiltonian for the $U(1)$ lattice gauge theory takes the form

$$H = U \sum_{o} \left(S_o^z\right)^2 - J \sum_{p} B_p + V N_{RK} \qquad (4)$$

where the first term in the Hamiltonian defines a low-energy sector consisting of allowed spin configurations with an equal number of up and down spins on each octahedron, that is, spin configurations with vanishing total spin $S_o^z = \sum_{i \in o} \sigma_i^z$ on each octahedron. The second term denotes a ring exchange interaction on each plaquette with $B_p = S_1^+ S_2^- S_3^+ S_4^- + S_1^- S_2^+ S_3^- S_4^+$; here $S_i^{\pm} = [\sigma_i^x \pm i\sigma_i^y]/2$ and the numbering is clockwise around the plaquette. This term flips a state with alternating up and down spins on a plaquette, that is, $|\uparrow, \downarrow, \uparrow, \downarrow\rangle_p \rightarrow |\downarrow, \uparrow, \downarrow, \uparrow\rangle_p$. The last term denotes the so-called Rokhsar–Kivelson term, which counts the total number of flippable plaquettes $N_{RK} = \sum_p B_p^2$. Whereas the ring exchange interaction commutes with the spin constraint, ring exchange terms on neighbouring plaquettes are non-commuting. At the Rokhsar–Kivelson point, with $J = V$, the system becomes exactly solvable[35], and it has been proposed that in the regime $0 \leq V \leq J$ the ground state is determined by a spin liquid smoothly connected to the Rokhsar–Kivelson point[33]: the properties of this spin liquid are given by an artificial 'photon' mode, gapped excitations carrying an 'electric' charge (violation of the constraint on an octahedron), which interact with a $1/r$ Coulomb potential mediated by the artificial photons, and gapped magnetic monopoles.

In the following, we present the implementation of this Hamiltonian in our scheme for the digital quantum simulation and

**Figure 4 | Lattice gauge theory. a**, Illustration of a dimer covering with three dimers (red links) meeting at each site of the cubic lattice. The front plaquette represents a flippable plaquette, which is transformed under the action of the ring-exchange $B_p$ into a different dimer covering. **b**, Numerical simulation for the cooling into the ground state at the Rokhsar–Kivelson point with $E = 0$ for a system with four unit cells (12 spins). The cooling into the constraint on the octahedra follows in analogy to the cooling of the toric code through the diffusion and annihilation of 'electric charges' on the octahedra. The inset shows the cooling into the equal superposition of all dimer coverings starting from an initial state satisfying the constraint on all octahedra. **c**, Coherent time evolution from the Rokhsar–Kivelson point with a linear ramp of the Rokhsar–Kivelson term $V(t) = J(1 - tJ/10\hbar)$: the solid line denotes the exact ground-state energy and the dots represent the digital time evolution during an adiabatic ramp for different phases $\phi$ written during each time step. The difference accounts for errors induced by the Trotter expansion because of the non-commutative terms in the Hamiltonian.

demonstrate that dissipative ground-state cooling can be achieved at the Rokhsar–Kivelson point. The control qubits reside in the centre of each octahedron (on the lattice sites of the 3D cubic lattice) controlling the interaction on each octahedron, and in the centre of each plaquette for the ring exchange interaction $B_p$, see Fig. 1. Then, the coherent time evolution of the Hamiltonian (4) can be implemented in analogy to the above discussion by noting that the ring exchange interaction $B_p$ and $N_{RK}$ can be written as a sum of four-body interactions of the form (3), whereas the constraint on the octahedra is an Ising interaction, see the Methods section. Next, we discuss the jump operators for the dissipative ground-state preparation. The cooling into the subspace with an equal number of up and down spins on each octahedron is obtained by the jump operator

$$ c_s = \frac{1}{4}\left[ 1 + \prod_j e^{-i\frac{\pi}{6}\sigma_j^z} \right] \sigma_i^x \left[ 1 - \prod_j e^{i\frac{\pi}{6}\sigma_j^z} \right] $$

where the product is carried out over the six spins located on the corners of the octahedron (see Fig. 1d). The 'interrogation' part $1 - \prod_j \exp(i(\pi/6)\sigma_j^z)$ of the jump operator vanishes if applied to any state with three up and three down spins, whereas in all other cases a spin is flipped. Then, the cooling follows in analogy to the cooling in the toric code by the diffusion of the 'electric' charges. Identifying each spin up with a 'dimer' on the link, all states satisfying the constraints on the octahedra can be viewed as

a dimer covering, with three dimers meeting at each site of the cubic lattice, see Fig. 4a. In this description, the ground state at the Rokhsar–Kivelson point is given by the condensation of the dimer coverings[34], that is, the equal-weight superposition of all dimer coverings. The condensation of the dimer coverings is then achieved by the jump operator

$$ c_p = \frac{1}{2}\sigma_i^z \left[ 1 - B_p \right] B_p $$

This jump operator has two dark states, which are the 0 and $+1$ eigenstates of $B_p$. The 0 eigenstate corresponds to a non-flippable plaquette, whereas the $+1$ eigenstate is the equal-weight superposition of the original dimer covering and the dimer covering obtained by flipping the plaquette (that is, the $+1$ eigenstate). Finally, the jump operator $c_p$ transforms the third eigenstate, with eigenvalue $-1$, into the $+1$ eigenstate. After acting on all plaquettes, the system is cooled into the dark state, which is the equal superposition of all dimer coverings, which can be reached by flipping different plaquettes. The cooling of these jump operators is demonstrated using a numerical simulation for a small system of four unit cells, see Fig. 4b.

The implementation of the digital quantum simulations provides full control on the spatial and temporal interaction strengths. Therefore, there are two possibilities to analyse the phase diagram for arbitrary interaction strengths. The possibility to vary the different coupling strengths in time enables us adiabatically to explore the phase diagram; the adiabatic preparation using the Trotter expansion is shown in Fig. 4c. On the other hand, the spatial control of the coupling parameters enables us to divide the lattice into a system and a bath. The ground state of the bath is given by the Rokhsar–Kivelson state, which can be continuously cooled through the dissipative terms, and the system part is sympathetically cooled because of its contact with the bath; in analogy to the cooling well known in condensed-matter systems.

## Methods

**Gate errors.** In the following, we discuss the influence of a gate error on the dynamics of the system. For simplicity, we illustrate the general behaviour for an error in the many-body gate $U_g$ for the coherent time evolution of the many-body interaction $A_p$. The imperfect many-body gate operation can be written

$$ \tilde{U}_g = |0\rangle\langle 0|_c \otimes e^{i\phi Q} + |1\rangle\langle 1|_c \otimes A_p \tag{5} $$

where the perfect gate $U_g$ is recovered for $Q \to 0$ and the operator $Q = Q^\dagger$ acts on the system spins surrounding the control atom. This form of the error is motivated by the specific implementation of the gate[11]; however, it can be seen that different errors in the many-body and single-particle gates will lead to similar phenomena. For the coherent time evolution, the imperfect gate gives rise to a finite amplitude for the control qubit to end up in the state $|1\rangle_c$. Consequently, optical pumping of the control qubit is required to reinitialize the system. Then the gate operations on a single plaquette give rise to the mapping of the density matrix onto

$$ \rho \to C\rho C^\dagger + D\rho D^\dagger $$

with ($\Theta \equiv e^{i\phi Q}$)

$$ C = \frac{1}{2}\left[ (\Theta^2 + 1)\cos\phi + (\Theta A_p + A_p \Theta)i\sin\phi \right] $$
$$ \approx \exp\left[ i\phi(A_p + Q) \right] - \frac{\phi^2}{2}Q^2 $$
$$ D = \frac{1}{2}\left[ (\Theta^2 - 1)\cos\phi + (\Theta A_p - A_p \Theta)i\sin\phi \right] $$
$$ \approx -i\phi Q $$

The last equations hold with an accuracy up to third order in the small parameter $\phi$. Consequently, the optical pumping has no influence in leading order, and the system is well described by a Hamiltonian evolution with the modified Hamiltonian $H = -(\hbar/\tau)\phi[A_p + Q]$. The characteristic energy scale of the correction is again given by $\hbar\phi/\tau$, and consequently describes a small perturbation if $|Q| \ll 1$.

In the second-order expansion in the small parameter $\phi$, the mapping of the density matrix reduces to

$$\rho \rightarrow \rho - i\phi[h, \rho] - \frac{\phi^2}{2}[h, [h, \rho]] + \frac{\phi^2}{2}\left(2Q\rho Q - \{Q^2, \rho\}\right)$$

with $h = -[A_p + Q]$. The first terms on the right-hand side describe the coherent evolution of the system with the evolution operator $\exp(-i\phi h)$ consistently expanded up to second order, whereas the last term takes the standard Lindblad form for a dissipative coupling, with the jump operator $c_e = Q$ describing a dephasing with the rate $\kappa_e = \phi^2/\tau$.

**Mesoscopic Rydberg gate.** In the following we briefly summarize the main properties and requirements of the many-body Rydberg gate $U_g$ introduced in ref. 11. The internal level structure of the control atom and the surrounding ensemble atoms is depicted in Fig. 1. The underlying physical mechanism of the gate operation (2) is a conditional Raman transfer of all ensemble atoms between their logical internal states $|A\rangle$ and $|B\rangle$, which—depending on the internal state $|0\rangle$ or $|1\rangle$ of the control qubit—is either inhibited or enabled. The gate is realized by the following three laser pulses. (i) A first state-selective $\pi$-pulse acting on the control atom changes the ground state $|1\rangle$ into the Rydberg state $|r\rangle$. (ii) During the whole gate operation, a strong-coupling laser of Rabi frequency $\Omega_c$ constantly acts on all ensemble atoms and off-resonantly couples the Rydberg level $|R\rangle$ to the intermediate level $|P\rangle$ with a detuning $\Delta$. Its frequency is chosen such that it is in two-photon resonance with the two Raman laser beams of Rabi frequency $\Omega_p$ (see Fig. 1), thereby establishing a condition known as electromagnetically induced transparency[36]. The system then adiabatically follows a zero-energy dark state, which at the end of the pulse is identical to the one at the beginning. In consequence, when the Raman laser pulses are applied—and provided the control atom resides in state $|0\rangle$—this two-photon resonance condition effectively blocks the Raman transfer from $|A\rangle$ to $|B\rangle$. In the case that the control atom was excited to the Rydberg state $|r\rangle$ in step (i), the large Rydberg–Rydberg interaction energy shift (dipole blockade) lifts the blocking condition for the ensemble atoms and thus the Raman transfer takes place. (iii) Finally, the control atom is transferred from state $|r\rangle$ back to $|1\rangle$ through a second $\pi$-pulse. The total time $T_{gate}$ required for the gate is mainly limited by the duration of the Raman pulse, resulting in $T_{gate} \sim 16\pi\Delta/(3\Omega_p^2)$. The principal error source for the many-body gate is due to the Rydberg–Rydberg interactions between the ensemble atoms. For $N$ ensemble atoms the accumulated phase errors scale as $\phi|Q| \sim N(N-1)(\Omega_p/\Omega_c)^2$, that is, they depend on all possible pair combinations and the probability of an ensemble atom being excited to the Rydberg state because of non-adiabatic processes[11].

**Experimental implementation.** Our set-up consists of control and ensemble atoms trapped in large-spacing optical lattices (see Fig. 1), so that single-site addressability can be achieved. To manipulate ensemble atoms independently, their spacing $a$ must be larger than the wavelength $\lambda_p$ of the Raman lasers for the many-body gate. Such a spatial resolution can be achieved by tightly focusing the laser beam, by using superlattice beams for the gate pulses, or subwavelength addressing techniques based on magnetic field gradients[37] or dark-state resonances[38]. Control and ensemble atoms can be distinguished spectroscopically, for example, by using different hyperfine states in two state-dependent lattices. A suitable set of parameters is determined by balancing the need for sufficiently large lattice spacing with at the same time strong Rydberg interactions for a fast and high-fidelity many-body gate.

We require the ensemble atoms to be separated by $a = 3.5\lambda_p \approx 1.5\,\mu m$ and a fast many-body gate with $T_{gate} = 1.5\,\mu s$ (which is much shorter than the decoherence times, for example, resulting from radiative decay of the Rydberg states). For $^{87}Rb$ this is achieved by choosing $\Omega_p = 2\pi \times 67$ MHz, $\Delta = 2\pi \times 2$ GHz, $\Omega_c = 2\pi \times 1$ GHz, an interaction strength of $V = 10\hbar\Omega_c^2/\Delta$, and using the Rydberg states $|r\rangle_c = |59s\rangle$ and $|R\rangle_i = |53s\rangle$, respectively. Note that for these Rydberg states the corresponding distances are still larger than the LeRoy radius, that is, there is no overlap between the wavefunctions of the atoms. Furthermore, corrections to a pure van der Waals interaction because of resonant dipole–dipole couplings[39,40] are also small, and using $s$ states ensures the interaction is isotropic. For these parameters, the errors appearing from ensemble–ensemble interactions for $N = 4$ atoms result in $\phi|Q| = 0.2$.

Further errors arise from crosstalk between plaquettes being processed in parallel, that is, when a control atom interacts with ensemble atoms of distant plaquettes. As a result of the rapid decay of the van der Waals interaction the residual interaction is reduced by a factor of at least 125 on a square lattice. For $V = 10\hbar\Omega_c^2/\Delta$, the resulting error is of a similar size to that resulting from ensemble–ensemble interactions. This error can be further reduced by increasing the number of sublattices $z$ such that only every second or third plaquette is processed in parallel.

**Quantum gates for the $U(1)$ lattice gauge theory.** The Hamiltonian giving rise to the constraint for the spins on the octahedra can be expressed as a sum of Ising interactions,

$$(S_o^z)^2 = \sum_{i \neq j}^{6} \sigma_i^z \sigma_j^z + const$$

which allow for an efficient implementation using the general toolbox for quantum simulation. The implementation for the jump operators for the constraint is obtained in analogy to the general jump operators with the many-body gate $U_g$ replaced by the gate $|0\rangle\langle 0|_c \otimes \mathbf{1} + |1\rangle\langle 1|_c \otimes \prod_i \exp(i(\pi/6)\sigma_i^z)$. On the other hand, the ring exchange interaction can be written as a sum of commuting four-body interactions

$$\begin{aligned}
B_p &= \frac{1}{8}\sum_{j=1}^{8} B_p^{(j)} = \frac{1}{8}(\sigma_1^x \sigma_2^x \sigma_3^x \sigma_4^x + \sigma_1^y \sigma_2^y \sigma_3^y \sigma_4^y \\
&+ \sigma_1^x \sigma_2^x \sigma_3^y \sigma_4^y + \sigma_1^y \sigma_2^y \sigma_3^x \sigma_4^x - \sigma_1^x \sigma_2^y \sigma_3^x \sigma_4^y \\
&- \sigma_1^y \sigma_2^x \sigma_3^y \sigma_4^x + \sigma_1^x \sigma_2^y \sigma_3^y \sigma_4^x + \sigma_1^y \sigma_2^x \sigma_3^x \sigma_4^y)
\end{aligned}$$

Likewise, the Rokhsar–Kivelson term can be decomposed into

$$\begin{aligned}
B_p^2 &= \frac{1}{8}\sum_{j=1}^{8} N_p^{(j)} = \frac{1}{8}(\sigma_1^0 \sigma_2^0 \sigma_3^0 \sigma_4^0 - \sigma_1^0 \sigma_2^0 \sigma_3^z \sigma_4^z \\
&+ \sigma_1^0 \sigma_2^z \sigma_3^0 \sigma_4^z - \sigma_1^0 \sigma_2^z \sigma_3^z \sigma_4^0 - \sigma_1^z \sigma_2^0 \sigma_3^0 \sigma_4^z \\
&+ \sigma_1^z \sigma_2^0 \sigma_3^z \sigma_4^0 - \sigma_1^z \sigma_2^z \sigma_3^0 \sigma_4^0 + \sigma_1^z \sigma_2^z \sigma_3^z \sigma_4^z)
\end{aligned}$$

where $\sigma_i^0$ is the identity matrix. Consequently, the coherent time evolution again follows from the general toolbox, and the jump operators for cooling into the ground state at the Rokhsar–Kivelson point effectively cool into the zero eigenvalue eigenstate of the operators

$$\frac{1}{2}[1 - B_p]B_p = \frac{1}{16}\sum_{j=1}^{16} C_p^{(j)} = \frac{1}{16}\left[\sum_{j=1}^{8} B_p^{(j)} - \sum_{j=1}^{8} N_p^{(j)}\right]$$

This can be achieved by replacing the gate $U_g$ with

$$\begin{aligned}
U_B &= |0\rangle\langle 0|_c \otimes \mathbf{1} + |1\rangle\langle 1|_c \otimes \exp\left[i\frac{\pi}{2}(1 - B_p)B_p\right] \\
&= \prod_{j=1}^{16} U_c(\pi/2)^{-1} U_j U_c(\pi/2) \exp(i\pi/32\,\sigma_c^z) \\
&\times U_c(\pi/2)^{-1} U_j U_c(\pi/2)
\end{aligned}$$

with $U_j = |0\rangle\langle 0|_c \otimes \mathbf{1} + |1\rangle\langle 1|_c \otimes C_p^{(j)}$. This gate operation leaves states with eigenvalue $0$ or $+1$ of $B_p$ invariant, whereas the $-1$ eigenvalue picks up a phase of $\pi$. It can be implemented as a product of many-body gates which derive directly from the standard gate $U_g$ with the combination of spin rotations.

## References

1. Gallagher, T. F. *Rydberg Atoms* (Cambridge Univ. Press, 1994).
2. Tong, D. *et al.* Local blockade of Rydberg excitation in an ultracold gas. *Phys. Rev. Lett.* **93,** 063001 (2004).
3. Singer, K., Reetz-Lamour, M., Amthor, T., Marcassa, L. G. & Weidemüller, M. Suppression of excitation and spectral broadening induced by interactions in a cold gas of Rydberg atoms. *Phys. Rev. Lett.* **93,** 163001 (2004).
4. Cubel, T. *et al.* Coherent population transfer of ground-state atoms into Rydberg states. *Phys. Rev. A* **72,** 023405 (2005).
5. Vogt, T. *et al.* Dipole blockade at Förster resonances in high resolution laser excitation of Rydberg states of cesium atoms. *Phys. Rev. Lett.* **97,** 083003 (2006).
6. Mohapatra, A. K., Jackson, T. R. & Adams, C. S. Coherent optical detection of highly excited Rydberg states using electromagnetically induced transparency. *Phys. Rev. Lett.* **98,** 113003 (2007).
7. Heidemann, R. *et al.* Evidence for coherent collective Rydberg excitation in the strong blockade regime. *Phys. Rev. Lett.* **99,** 163601 (2007).
8. Nelson, K. D., Li, X. & Weiss, D. S. Imaging single atoms in a three-dimensional array. *Nature Phys.* **3,** 556–560 (2007).
9. Whitlock, S., Gerritsma, R., Fernholz, T. & Spreeuw, R. J. C. Two-dimensional array of microtraps with atomic shift register on a chip. *New J. Phys.* **11,** 023021 (2009).
10. Møller, D., Madsen, L. B. & Mølmer, K. Quantum gates and multiparticle entanglement by Rydberg excitation blockade and adiabatic passage. *Phys. Rev. Lett.* **100,** 170504 (2008).
11. Müller, M., Lesanovsky, I., Weimer, H., Büchler, H. P. & Zoller, P. Mesoscopic Rydberg gate based on electromagnetically induced transparency. *Phys. Rev. Lett.* **102,** 170502 (2009).

12. Gaëtan, A. *et al.* Observation of collective excitation of two individual atoms in the Rydberg blockade regime. *Nature Phys.* **5,** 115–118 (2009).
13. Urban, E. *et al.* Observation of Rydberg blockade between two atoms. *Nature Phys.* **5,** 110–114 (2009).
14. Breuer, H.-P. & Petruccione, F. *The Theory of Open Quantum Systems* (Oxford Univ. Press, 2002).
15. Feynman, R. P. Simulating physics with computers. *Int. J. Theor. Phys.* **21,** 467–488 (1982).
16. Lloyd, S. Universal quantum simulators. *Science* **273,** 1073–1078 (1996).
17. Kitaev, A. Y. Fault-tolerant quantum computation by anyons. *Ann. Phys.* **303,** 2–30 (2003).
18. Diehl, S. *et al.* Quantum states and phases in driven open quantum systems with cold atoms. *Nature Phys.* **4,** 878–883 (2008).
19. Kraus, B. *et al.* Preparation of entangled states by quantum Markov processes. *Phys. Rev. A* **78,** 042307 (2008).
20. Aguado, M., Brennen, G. K., Verstraete, F. & Cirac, J. I. Creation, manipulation, and detection of Abelian and non-Abelian anyons in optical lattices. *Phys. Rev. Lett.* **101,** 260501 (2008).
21. Bombin, H. & Martin-Delgado, M. A. Topological quantum distillation. *Phys. Rev. Lett.* **97,** 180501 (2006).
22. Kitaev, A. Y. Anyons in an exactly solved model and beyond. *Ann. Phys.* **321,** 2–111 (2006).
23. Duan, L.-M., Demler, E. & Lukin, M. D. Controlling spin exchange interactions of ultracold atoms in optical lattices. *Phys. Rev. Lett.* **91,** 090402 (2003).
24. Jackeli, G. & Khaliullin, G. Mott insulators in the strong spin–orbit coupling limit: From Heisenberg to a quantum compass and Kitaev models. *Phys. Rev. Lett.* **102,** 017205 (2009).
25. Sørensen, A. & Mølmer, K. Spin–spin interaction and spin squeezing in an optical lattice. *Phys. Rev. Lett.* **83,** 2274–2277 (1999).
26. Bloch, I., Dalibard, J. & Zwerger, W. Many-body physics with ultracold gases. *Rev. Mod. Phys.* **80,** 885–964 (2008).
27. Vidal, J., Dusuel, S. & Schmidt, K. P. Low-energy effective theory of the toric code model in a parallel magnetic field. *Phys. Rev. B* **79,** 033109 (2009).
28. Fölling, S. *et al.* Spatial quantum noise interferometry in expanding ultracold atom clouds. *Nature* **434,** 481–484 (2005).
29. Altman, E., Demler, E. & Lukin, M. D. Probing many-body states of ultracold atoms via noise correlations. *Phys. Rev. A* **70,** 013603 (2004).
30. Kogut, J. B. An introduction to lattice gauge theory and spin systems. *Rev. Mod. Phys.* **51,** 659–713 (1979).
31. Moessner, R. & Sondhi, S. L. Resonating valence bond phase in the triangular lattice quantum dimer model. *Phys. Rev. Lett.* **86,** 1881–1884 (2001).
32. Motrunich, O. & Senthil, T. Exotic order in simple models of bosonic systems. *Phys. Rev. Lett.* **89,** 277004 (2002).
33. Hermele, M., Fisher, M. P. A. & Balents, L. Pyrochlore photons: The $U(1)$ spin liquid in a $S = 1/2$ three-dimensional frustrated magnet. *Phys. Rev. B* **69,** 064404 (2004).
34. Levin, M. & Wen, X.-G. Colloquium: Photons and electrons as emergent phenomena. *Rev. Mod. Phys.* **77,** 871–879 (2005).
35. Rokhsar, D. & Kivelson, S. Superconductivity and the quantum hard-core dimer gas. *Phys. Rev. Lett.* **61,** 2376–2379 (1988).
36. Fleischhauer, M., Imamoglu, A. & Marangos, J. P. Electromagnetically induced transparency: Optics in coherent media. *Rev. Mod. Phys.* **77,** 633–673 (2005).
37. Stokes, K. D. *et al.* Precision position measurement of moving atoms using optical fields. *Phys. Rev. Lett.* **67,** 1997–2000 (1991).
38. Gorshkov, A. V., Jiang, L., Greiner, M., Zoller, P. & Lukin, M. D. Coherent quantum optical control with subwavelength resolution. *Phys. Rev. Lett.* **100,** 093005 (2008).
39. Li, W., Tanner, P. J. & Gallagher, T. F. Dipole–dipole excitation and ionization in an ultracold gas of Rydberg atoms. *Phys. Rev. Lett.* **94,** 173001 (2005).
40. Walker, T. G. & Saffman, M. Consequences of Zeeman degeneracy for the van der Waals blockade between Rydberg atoms. *Phys. Rev. A* **77,** 032723 (2008).

## Author contributions

All five authors contributed equally to all parts of this work.

## Additional information

The authors declare no competing financial interests. Reprints and permissions information is available online at http://npg.nature.com/reprintsandpermissions. Correspondence and requests for materials should be addressed to H.W.